Icarus **160**, 161–171 (2002)
doi:10.1006/icar.2002.6962

Moonlet Collisions and the Effects of Tidally Modified Accretion in Saturn's F Ring

John M. Barbara[1] and Larry W. Esposito

Laboratory for Atmospheric and Space Physics, University of Colorado, 392 UCB, Boulder, Colorado 80309-0392
E-mail: jbarbara@giss.nasa.gov

Received July 20, 2000; revised June 17, 2002

We both test and offer an alternative to a meteoroid bombardment model (M. R. Showalter 1998, *Science* 282, 1099–1102) and suggest that anomalous localized brightenings in the F ring observed by *Voyager* result from disruptive collisions involving poorly consolidated moonlets, or "rubble piles." This model can also explain the transient events observed during ring plane crossing. We have developed an evolutionary model that considers both the competing effects of accretion and disruption at the location of the F ring. Our numerical model is a Markov process where probabilities of mass transfer between the states of the system form a "transition matrix." Successive multiplications of this matrix by the state vector generate expectation values of the distribution after each time step as the system approaches quasi-equilibrium. Competing effects of accretion and disruption in the F ring are found to lead to a bimodal distribution of ring particle sizes. In fact, our simulation predicts the presence of a belt of kilometer-sized moonlets in the F ring. These moonlets may continually disrupt one another and re-accrete on short time scales. We also agree with J. N. Cuzzi and J. A. Burns (1988, *Icarus* 74, 284–324), who suggest that the classical F ring itself may be the consequence of a relatively recent collision between two of the largest of these yet unseen objects. *Cassini* observations can confirm the existence of the moonlet belt by directly observing these objects or the waves they create in the rings.

Key Words: **planetary rings, Saturn; Saturn.**

1. INTRODUCTION

Since its discovery in 1979, Saturn's F ring has long remained an enigma. Its unique location beyond the classical Roche limit, characteristic brightness variations, and braided strands have challenged our understanding of the processes that produce and shape the elaborate ring systems of the outer planets. The F ring unmistakably defies the premise that a rigid division exists between the domains of rings and moons. While many of the ring's relatively stable structures have been attributed to gravitational perturbations induced by the F-ring's "shepherding" moons, Prometheus and Pandora, the exact origin of a number of short-lived brightness enhancements or "burst" events witnessed during the 1980 and 1981 *Voyager* encounters remains obscure. This phenomenon was previously explained in terms of meteoroid bombardment of the ring (Showalter 1998). More recently, Poulet *et al.* (2000) have analyzed similar transient F-ring features observed in August and November 1995 during the Earth and Sun crossings of Saturn's ring plane and propose that these features may be clouds of regolith ejecta produced by collisions involving large "parent bodies" in the F ring. The presence of a population of moonlet scale objects (0.1–10 km radius) extending throughout the entire annulus between the F-ring shepherds was first inferred by Cuzzi and Burns (1988) based on their reconsideration of *Pioneer 11*'s detection of depletions in the flux of trapped magnetospheric electrons. Of five observed depletions, only two were probably due to the known F ring. Cuzzi and Burns proposed that collisions between these unseen objects cause them to shed regolith material from their surfaces, thereby producing the microsignature depletions. If the belt consists entirely of 10-km radius moonlets, they estimate a total count of ∼10,000 bodies. For a belt made up entirely of 100-m-radius moonlets, they estimate a total count of ∼100 million. Realistically, they suggest, the moonlets should follow some size distribution within these constraints, which are imposed by the fact that the moonlets must exceed the mass of a typical clump; yet *Voyager*'s camera should have detected any object with radius exceeding approximately 10 km.

The intent of this body of work is to test and evaluate the validity of a meteoroid impact model and provide an alternative explanation for transient F-ring features. Our model is quite similar to that of Poulet *et al*. (2000) with the exception that we explicitly consider the evolution of a complete size distribution under the effects of both accretion and fragmentation in the F ring. We argue that the complete disruption of these larger moonlets, which are assumed to be loosely bound, may give rise to the "burst" events witnessed by Showalter and to the visually prominent features later observed during the Earth and Sun crossings of Saturn's ring plane.

While traditional accretion simulations predict the rapid formation of single satellites from ring particles on relatively short time scales, theories of ring formation have generally dismissed

[1] Now at SGT, Inc./NASA—Goddard Institute for Space Studies, 2880 Broadway, New York, NY 10025.

0019-1035/02 $35.00

the process of accretion within the classical Roche limit altogether. This dichotomous view of planetary ring and moon environments proves grossly oversimplified in view of the continued coexistence of rings and small satellites. Simulations in the broad "tidally modified" region surrounding the classical Roche limit have suggested that accretion results only from those bodies whose masses differ substantially (Canup and Esposito 1995). By contrast, two bodies with similar mass will exceed their mutual Hill sphere (Ohtsuki 1993) and fail to become gravitationally bound. Similar simulations also suggest that tidally modified accretion can lead to a bimodal size distribution of ring particles.

We have developed a self-consistent numerical model that accounts for the processes of accretion and disruption valid in the F-ring environment. Our major results indicate that: (1) the steep power-law distribution of impacting meteoroids at the location of the F ring would suggest many burst events smaller than those observed by *Voyager*; (2) competing effects of accretion and disruption in the F ring environment lead toward a bimodal distribution of sizes, lending support to theories of a persistent population of yet unseen moonlets; and (3) the combination of a bimodal distribution of ring bodies and size-dependent disruptions reflects a threshold for burst events akin to *Voyager* observation.

Section 2 describes our Monte Carlo representation of the meteoroid impact model and apparent inconsistencies found between the model and observation. Our numerical moonlet collision model is discussed in Section 3. Section 4 presents our major results, with a discussion and final conclusions following in Section 5.

2. METEOROID IMPACT MODEL

From a detailed analysis of some 1500 *Voyager* images, Showalter (1998) has derived longitudinal profiles of the F ring's radially integrated intensity. Of the many regions of enhanced intensity, or "clumps," all but three were found to be relatively stable, exhibiting only minor visible evolution over periods of about 1 to 2 months. These three exceptions, although rivaling the intensities of some of the brightest stable clumps, had lifetimes far shorter than the majority of the ring's features, appearing in a matter of days and fading in ~2 weeks or so; for this reason they have been dubbed "burst events." Within about 15 days of *Voyager*'s closest approaches, such events should have been readily visible; with two encounters (*Voyager I* and *II*) and three detected events, they occur with a frequency of approximately one per 20 days.

As observed by Showalter, the spreading rates of the burst events imply a random particle motion of $\sim 4\ \mathrm{m\ s^{-1}}$. Considering the F ring's core is only a few kilometers wide, he reasoned that these events are caused by external hypervelocity impacts, rather than resulting from mutual collisions of F-ring bodies—where velocities have been taken to be much lower. Figure 1 illustrates three bright clumps detected by *Voyager*. Events 2B, 2C', and 2C represent stable, long-lived clumps. The feature marked 2A is one of the three detected burst events. The top panel of Fig. 1 was derived from 28 images taken ~5 days before *Voyager II*'s closest approach; the bottom panel was derived from 8 images obtained ~4 days after.

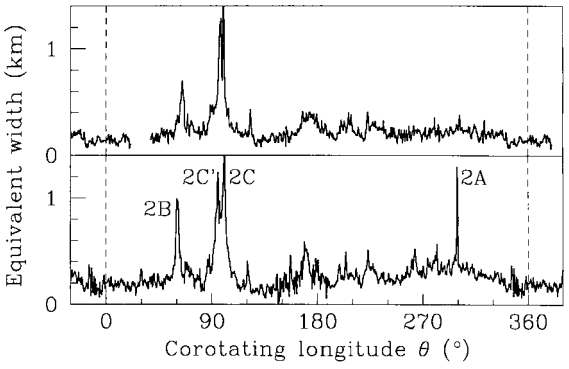

FIG. 1. Complete longitudinal profiles of the F ring from the *Voyager 2* encounter. Events 2B, 2C′, and 2C represent stable, long-lived clumps. The event marked 2A is one of the three detected "burst events" (Showalter 1998).

Estimating relative amounts of dust released from hypervelocity impacts, Showalter (1998) concluded that impactors with radii on the order of 10 cm colliding with ring particles are the most plausible source of burst events, estimating the frequency for such a collision as every 60 days. If the meteoroid impact model is accurate, the F ring could become the Solar System's best detector of meteoroids in this size range; the ring's optical depth τ, ~0.1, offers a substantial target for impactors; yet the ring remains optically thin enough that the resulting injection of dust may be perceived as a noticeable event.

We use a Monte Carlo method to simulate the meteoroid impact model, with impactors drawn randomly from a power-law size distribution of the form

$$n(r)\,dr \propto r^{-q}, \tag{1}$$

where $n(r)\,dr$ is the number of impactors in the size range r to $r + dr$, and q is the power-law exponent. Near the F ring, $2.5 \le q \le 4.5$ (Showalter 1998).

In this stochastic model, we set the mean time between impacts resulting from one 10-cm meteoroid to 60 days. Once an event has been detected, it is assigned to a random longitude on the ring, where the excess brightness of the event is proportional to the impactor's mass, or radius cubed. The intensity, I, resulting from a 10-cm-radius impactor is given a value of $I = 1$. According to this scale, an event involving an 8-cm meteoroid will produce an intensity $I \approxeq 0.5$. Simulation results are then plotted on a graph of intensity versus longitude (see Fig. 2) where the observer is placed at a corotating reference point, thereby allowing ring features to remain essentially motionless. It is worth noting that this model does not include any of the other stable features of the ring. We consider only burst events similar to that marked 2A in Fig. 1, and, as evidenced by this

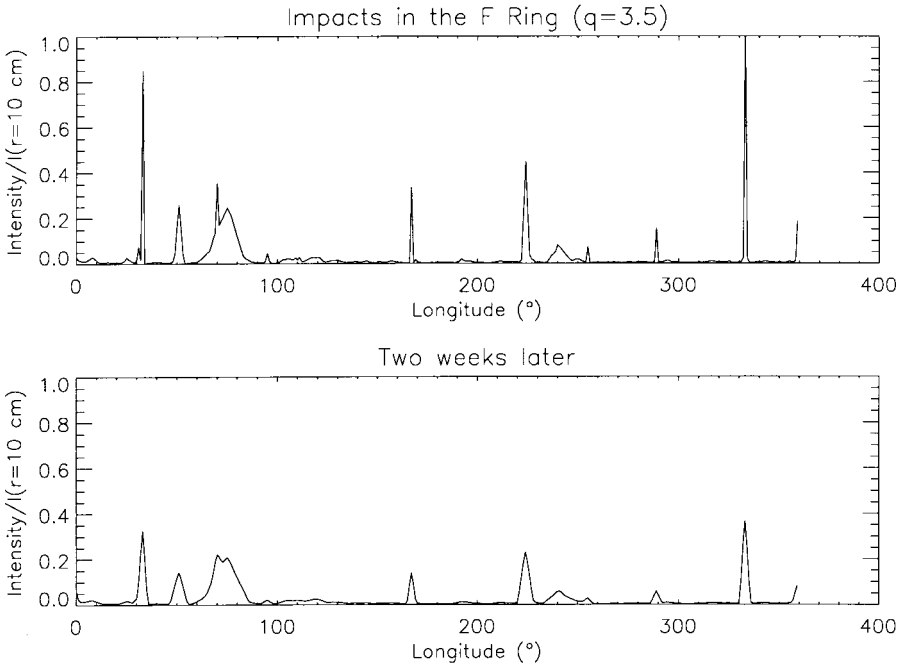

FIG. 2. Meteoroid impacts, plotted as a function of longitude, produced by a Monte Carlo simulation with impactors drawn randomly from a continuous power law with exponent equal to 3.5. Intensities, I, equal to 1 correspond to collisions involving a 10-cm-radius impactor.

profile, the F ring is azimuthally clumpy, irregular, and much noisier than the simplified picture we present in Fig. 2.

We include a decay process by treating an event as a triangle whose base spreads in full width by the observed 0.3° per day (Showalter 1998). The triangle's overall area is conserved; the result is a linear decrease of intensity with time. The graphs represent a "snapshot" of the F ring at the end of some N number of days. In an attempt to create a situation analogous to the observations of *Voyager*, we typically run the program for 60 days. The simulation is a completely stochastic representation of the meteoroid impact model.

We conclude that our numerical simulation results are inconsistent with *Voyager*'s observation of burst events. While only a few relatively large isolated features have been observed in the F ring, our plots reveal numerous events generated by impacts involving smaller meteoroids, a residual effect of the steep power-law distribution of impactors near the ring. Figure 2 illustrates typical results where the power-law exponent for impeding meteoroids is equal to 3.5. We have also considered more conservative values for the power-law exponent q; however, the numerous smaller events remain plainly visible (see Fig. 3, where $q = 3.0$). Although the authors of this manuscript recognize that many of these much smaller events would remain unseen when superimposed upon the F ring's complex structure, we maintain that it would be difficult to hide all of these numerous dimmer events. Our comparisons of Figs. 1, 2, and 3 force us to the conclusion that an explanation for the F-ring features in terms of a purely meteoric origin is unlikely. *Cassini* observations will surely resolve this issue of the abundance of smaller burst events.

3. MOONLET COLLISION MODEL

Alternatives to a meteoroid impact model must afford adequate justification for the relatively high spreading rates—the very observation that led to an external foundation of burst event generation. We argue a combination of three significant processes crucial to explaining the relatively rapid spreading rates of the F-ring features: (1) individual particle dispersion velocities, (2) effects of Keplerian shear, and (3) sweep-up of dust by larger "parent" bodies. Traditionally, dispersion velocities, or rebound velocities, are given by

$$v_{\text{reb}} = \varepsilon \cdot v_i \tag{2}$$

where ε is the coefficient of restitution with a value equal to some constant between 0 and 1 (0 for a completely inelastic collision and 1 for a completely elastic collision), and v_i is the collision velocity (Canup and Esposito 1995). Dispersion velocities may also be modestly estimated by adopting a value equal to the escape velocity of the target: were the rebound velocity significantly less, the moonlet could not be disrupted. Escape velocities for a 10- and a 1-km-radius object are $\sim$7 and $\sim$1 m s^{-1}, respectively.

At the distance of the F ring, estimates of relative shearing velocities give a value of only $\sim$1 m s^{-1} across the 20-km diameter of a 10-km-radius moonlet.

Average sweep-up times for dust particles can be roughly estimated by

$$\Delta t = P/\tau, \tag{3}$$

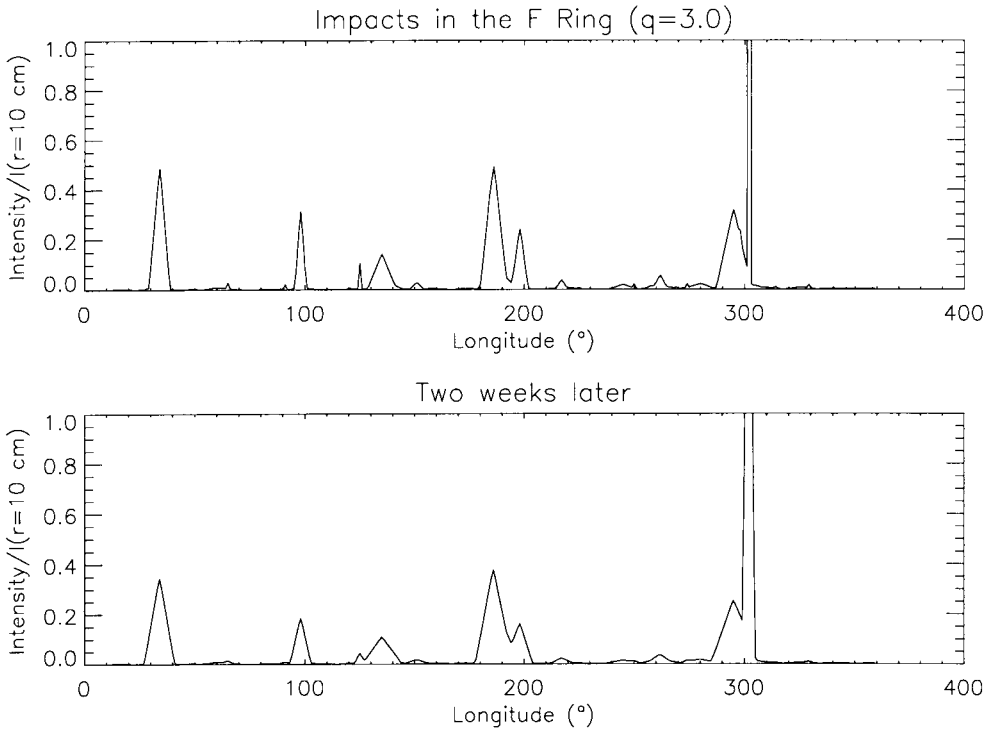

FIG. 3. As described in the legend to Fig. 2, but with a more conservative power-law exponent equal to 3.0.

where P is the orbital period for dust particles and τ is the ring's average optical depth. For the F ring, average dust sweep-up times are on the order of 10 days (Cuzzi and Burns 1988). These simple considerations require that random velocity in the ring be greater than 4 m/s for at least some of the collisions. This is larger than expected from the observed strand width, but possible due to collisions of particles in different strands or excited by close passage to one of the shepherds, Pandora or Prometheus. A burst event in the F ring would have a lifetime of 10 days or so against sweep-up.

3.1. Model Description

While N-body simulations monitor individual particles, our approach is to track probabilities of mass transfer for binned intervals of an initially continuous mass distribution. The technique is analogous to that developed by Canup and Esposito (1995) with the addition that we incorporate the process of disruption. The model is described as a Markov process where an initial state vector is established by the sum mass in each of 25 size bins. A Markov process is a stochastic process without memory—the evolution of the system is dependent only on its current state, and not on the history of the realization of that state. Probabilities of mass transfer are calculated between all states of the system, and collectively this set of probabilities forms a "transition matrix." Multiplication of this matrix by the state vector generates *expectation values* of the distribution after the first time step, and so forth. Each column of the transition matrix corresponds to interactions between two mass bins. This technique of tracking expectation values avoids exhaustive computation of individual orbits for the substantial numbers of objects considered, in turn eliminating an upper limit on the total allowable number of objects considered.

3.2. Mass Evolution

Our simulation incorporates particle growth through accretion and size decrease through disruption. Due to the high velocity and unconsolidated bodies assumed, the possibility of rebound has been neglected. All moonlets with radii greater than 100 m are distributed according to a power law into 24 logarithmically spaced mass bins (bins 1 through 24). Bin 0, or the "dust bin," is a continuance of the power law and contains objects down to a radius of 10 μm—a minimum marking the smallest particles that can withstand the solar wind and various drag forces that act to preferentially remove the smallest dust particles (Colwell 1996). A 20-km upper bound was selected, providing a useful check on the realism of our model given that objects with radii greater than $\sim$15 km should not have escaped detection by *Voyager*. For accretion from the dust bin into bin 1, we calculate the transition probability, assuming a power-law distribution in the dust bin.

There are three possible types of transition in this model: (a) the first arising from collisions involving members of the moonlet population and resulting in either disruption or accretion; (b) the second from collisions between the members of the dust bin

and moonlets; (c) and the third from the interactions within the dust bin.

3.2.1. Modeling moonlet interactions: disruption. If two like-sized objects collide, the consequence may be the disruption of each. In this case, the diagonal elements of the transition matrix are reduced and positive entries made to the dust bin and each of the bins below the largest bin involved in the collision. After a disruptive event, mass is redistributed according to a power law. As discussed further in Section 4, we have considered a range of values for the power-law exponent, $q_{\rm ejecta}$. Due to the broad range of particle sizes covered by bin 0, a significant fraction of the disrupted material is placed in the dust bin (bin 0),

$$\delta_{\rm f} = \left(\int_{r_{\rm o}}^{r_{\rm u}} m^{1-q_{\rm m}}\, dm \right) \Big/ \left(\int_{r_{\rm l}}^{r_{\rm u}} m^{1-q_{\rm m}}\, dm \right), \qquad (4)$$

where $r_{\rm u}$ is the radius of the disrupted moonlet bin, $r_{\rm o}$ is the lower cutoff of bin 1 (100 m), $r_{\rm l}$ is the lower bound of the dust bin (10 μm), and $q_{\rm m}$ is the power-law exponent for the size distribution, also in terms of mass. For $q = 3.5$ (in terms of radius), $q_{\rm m} = 1.83$. Solving this equation yields $\delta_{\rm f} = 0.46$ for disruption of a 20-km moonlet. In other words, after a collision resulting in disruption, 46% of the mass is relocated into bin 0 and the remaining mass is distributed according to the power law throughout the remaining lower bins. It is worth noting that by increasing the value of the time step we could reduce the real computing time of our simulation. However, this model ignores multiple transitions in a single time step; therefore, time steps are carefully chosen to ensure that mass transfer never exceeds $\sim$1% per time step.

3.2.2. Modeling moonlet interactions: accretion. When two objects collide, the event will likely result in accretion if the bodies differ sufficiently in mass. Critical mass ratios for the accretion process are chosen in accordance with the results of Canup and Esposito (1995). We assume complete disruption after a collision for mass ratio below the critical value, and we assume complete accretion for values larger than the critical value. At the F ring's distance from Saturn, this critical mass ratio is $\sim$100 (see Canup and Esposito 1995, their Fig. 4a). Excluding events involving the largest bin, bin 24, the accreted mass is placed into successive bins, as calculated by integrating over the size distribution. In the case of events involving bin 24, all mass is restored to this bin.

3.2.3. Dust/Moonlet interactions. For collisions involving members of the dust bin and moonlets from the larger macroscopic mass bins, a loss entry is made in the dust row to account for its depletion. If the interaction involves bin 24, accreted mass is simply returned to that bin; otherwise the mass is placed into two successive bins to equal the lost dust mass, depleting the number of particles in the j bin by as many as are added to the $j+1$ bin. That is, some of the particles accreting dust are promoted into the next bin.

3.2.4. Dust/Dust interactions. In the moonlet collision simulation, the mass of colliding objects is taken as the average mass of the bins they occupy. We calculate a correction for particles within the dust bin that accounts for the largest dust particles growing by accretion into bin 1. We call this fraction of dust the "phantom" bin. It is the percentage of mass making up the dust bin that regulates the rate of mass transport from the dust bin into bin 1. We have tested the effect of this simplification by doubling and removing the phantom fraction; we find that the fraction adds only minimal amounts of mass to bin 1 (Fig. 4) and has no noticeable effect on bin 0—whose members present the greatest surface area and therefore drive the ring's average optical depth—or on the largest bins whose members trigger the pronounced visible events.

3.3. Collision Frequencies

We use the "particle-in-a-box" approximation to calculate collision probability, an effective representation in numerous accretion simulations. We have considered a broad range of values for the relative collisional velocities, $v_{\rm rel}$, from 1 up to 10 m s^{-1}, a value representative of velocities achieved by excitation from Prometheus and Pandora (Cuzzi and Burns 1988). Utilizing this particle-in-a-box approximation, the probability that two objects of mass m_1 and m_2 will collide and accrete per unit time is given by

$$A_{m1,m2} = (\alpha \cdot \sigma_{m1,m2} \cdot v_{\rm rel})/(2 \cdot \pi \cdot a \cdot W \cdot H), \qquad (5)$$

where α is the probability that the collision will result in accretion, $\sigma_{m1,m2}$ is the collisional cross section, a is the orbital semimajor axis, and H and W are the height and width of the "box," respectively. In this representation we consider a value of 60 km for both H and W. Accretion probability is governed by the critical mass ratio as described above (Canup and Esposito 1995). At the location of the F ring, the effects of gravitational focusing are negligible and are therefore ignored. The collisional cross section is then given by

$$\sigma_{m1,m2} = \left(\frac{3}{4}\right)^{\frac{2}{3}} \cdot \pi^{\frac{1}{3}} \cdot \rho^{-\frac{2}{3}} \cdot \left(m_1^{\frac{1}{3}} \cdot m_2^{\frac{1}{3}}\right)^2, \qquad (6)$$

where ρ is the particle density.

The system evolves in time via successive multiplications of the transition matrix until a slowly varying, nearly stable state is reached, yielding a quasi-stationary state distribution vector. Reminiscent of other simulations of tidally modified accretion, the resulting bimodal distribution is quite apparent (Canup and Esposito 1995). Figures 5a and 5b illustrate the final mass and number distributions of the system (results are discussed further in Section 4).

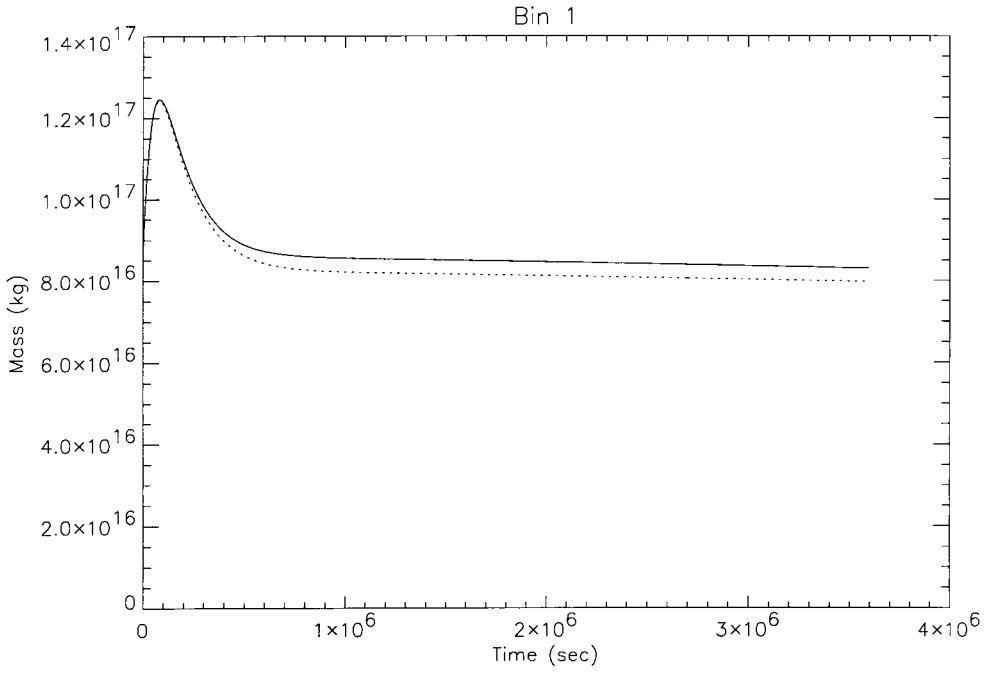

FIG. 4. Effects of the "phantom" fraction on the evolution of bin 1 mass as it approaches a quasi-stable state. Dotted line represents evolution of the system with the phantom fraction removed altogether.

4. RESULTS

4.1. Interpretation of Numerical Results

Our results indicate that the final bimodal distribution is not dependent on the initial size distribution. In fact, for all values of the initial power-law exponent, $1 \leq q_{\text{initial}} \leq 4.5$, final outcomes are wholly indistinguishable. However, the resultant distribution is quite sensitive to varying values of q_{ejecta}, the power-law exponent according to which mass is redistributed after a disruptive collision. With greater values of q_{ejecta}, the peak corresponding to the larger mode of the distribution (reflecting the average size of the moonlet population) is shifted toward larger particle radii. The greater mass of larger moonlets implies that increasing values of q_{ejecta} create moonlet belts containing less numerous yet larger moonlets, as evidenced by Fig. 6, where q_{ejecta} is taken as 3.0 (top panel) and 3.5 (bottom). In each case, the overall ring mass has been adjusted such that average optical depths remain at or close to 0.1. Note that for $q_{\text{ejecta}} \geq 3.5$, moonlets are completely absent.

In an attempt to recreate a scenario similar to that observed by *Voyager*, we have plotted the optical depth of the new state distribution of particles and the optical depth produced by collisions of the moonlets. Average optical depths have been calculated for all particles below the minimum illustrated in Fig. 5. To calculate the average optical depth produced by dust particles, τ_{d}, we consider

$$\tau_{\text{d}} = \int_{r_{\text{l}}}^{r_{\text{o}}} \pi \cdot r^2 \cdot n(r)\, dr, \tag{7}$$

where $n(r)\, dr$ is the number of particles in the size range r to $r + dr$, r_{l} is the lower bound of the dust bin (10 μm), and r_{o} is the upper bound of the dust bin.

Moonlets with radii exceeding the moonlet belt mass minimum have been placed randomly in longitude along the ring and their contributions to the optical depth are added to the average. Mass bins, including longitude, are then subjected to subsequent moonlet collisions to provide an instantaneous realization of the ring longitude brightness. Utilizing the current state vector and the collision frequencies calculated by the transition matrix, we calculate the number of events in each event bin per unit time. The sum of contributions from both dust and fragment distribution gives the cross-sectional area of an event and thus its optical depth, where, for the fraction that becomes dust, we consider

$$\tau_{\text{d}} = \int \pi \cdot r^2 \cdot n(r)\, dr \tag{8}$$

over all dust particle radii. For the larger macroscopic bodies created by the disruptive event, we consider

$$\sum_i n(r_i) \pi \cdot (r_i)^2. \tag{9}$$

Time steps are kept small and carefully regulated such that multiple events per step are negligible. At each time step, events are centered on the selected longitude and given a triangular pulse shape with a half-width proportional to the time elapsed since the occurrence of the event. The event area, or strength, A_{e}, is given by

$$A_{\text{e}} = \sum_i A_i \cdot \tau_i, \tag{10}$$

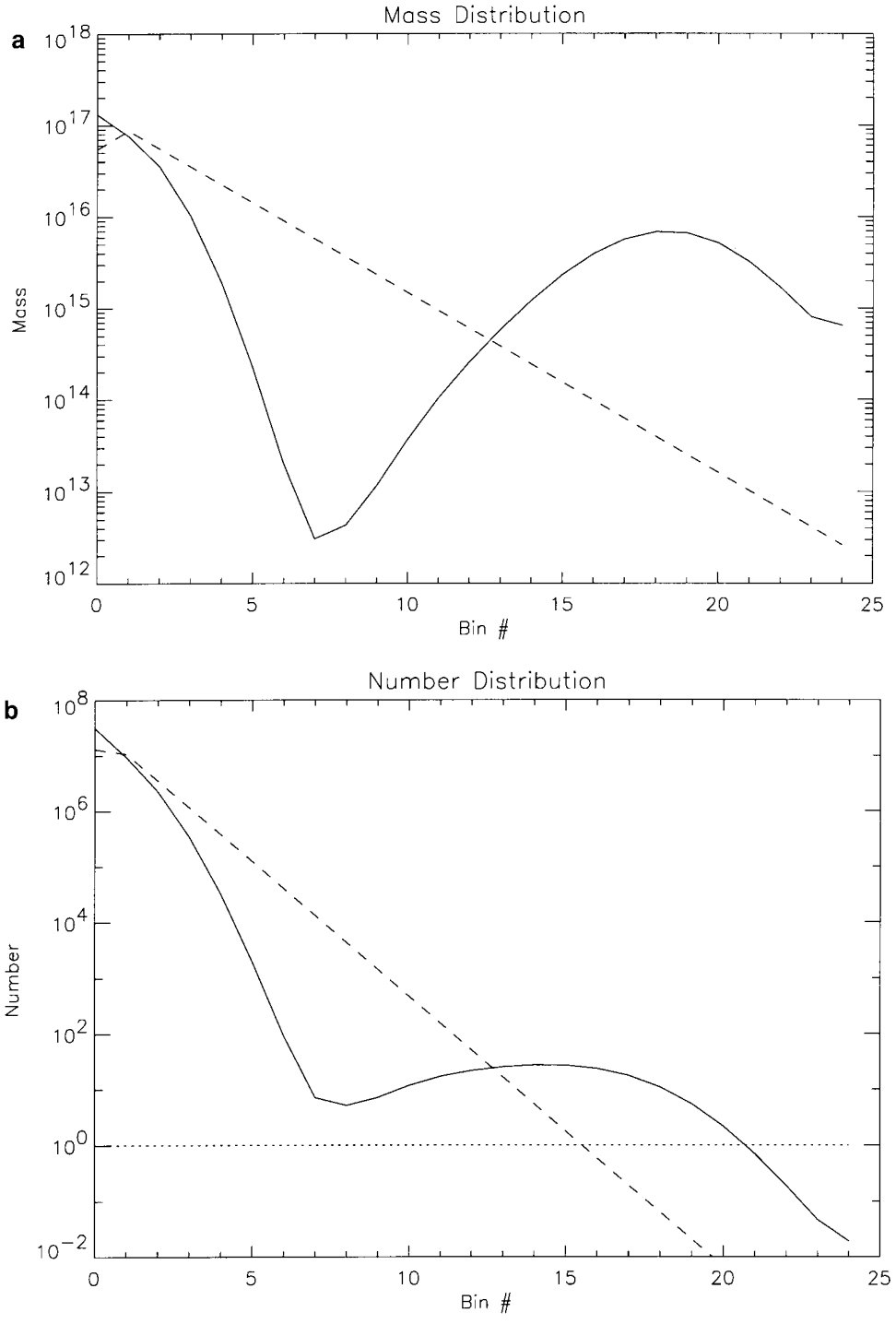

FIG. 5. Initial continuous power-law distribution (dashed) and final bimodal distributions for (a) mass and (b) number, where $q_{\text{ejecta}} = 3.1$ and overall F-ring mass has been modified such that the average optical depth remains equal to 0.1. The dotted line in (a) marks unity.

where A_i is the area of a sector, and τ_i is the optical depth contribution within that sector. Events are then added to the optical depth of the smaller particles and plotted as a function of longitude. Figure 7 illustrates representative results where $q_{\text{ejecta}} = 3.1$ and 5 m s^{-1} relative collision velocities are assumed. In this case three disruptive collisions result in localized visible events.

4.2. Relative Collision Velocities

As illustrated in Table I, accretion and disruption are governed by the mass ratio of colliding particles; only the system's sum number of collisions and rate of evolution toward equilibrium are affected by varying collision velocities while final state

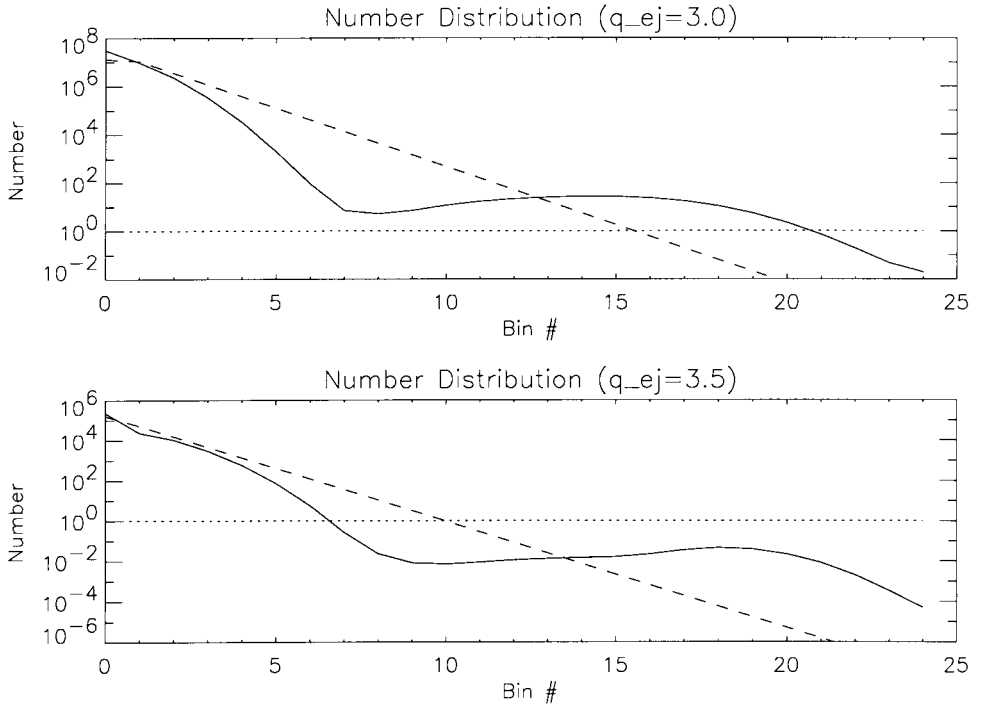

FIG. 6. Effects of varying q_{ejecta} on final number distributions for $q_{\text{ejecta}} = 3.0$ (top) and 3.5 (bottom). Note, for $q_{\text{ejecta}} = 3.5$, moonlets are absent entirely.

distribution vectors remain unchanged. Figure 8 demonstrates the evolution of mass in the ~8-km-radius bin for $v_{\text{rel}} = 10$ (solid), 5 (dotted), and 1 m s^{-1} (dashed). However, Fig. 9 reveals the intimate relationship between relative collision velocities and event frequency, with events becoming less and less frequent with decreasing relative collisional velocities. Thus the lower collision velocity provides a slower approach to the equilibrium distribution and slower spreading velocity for bright events. The

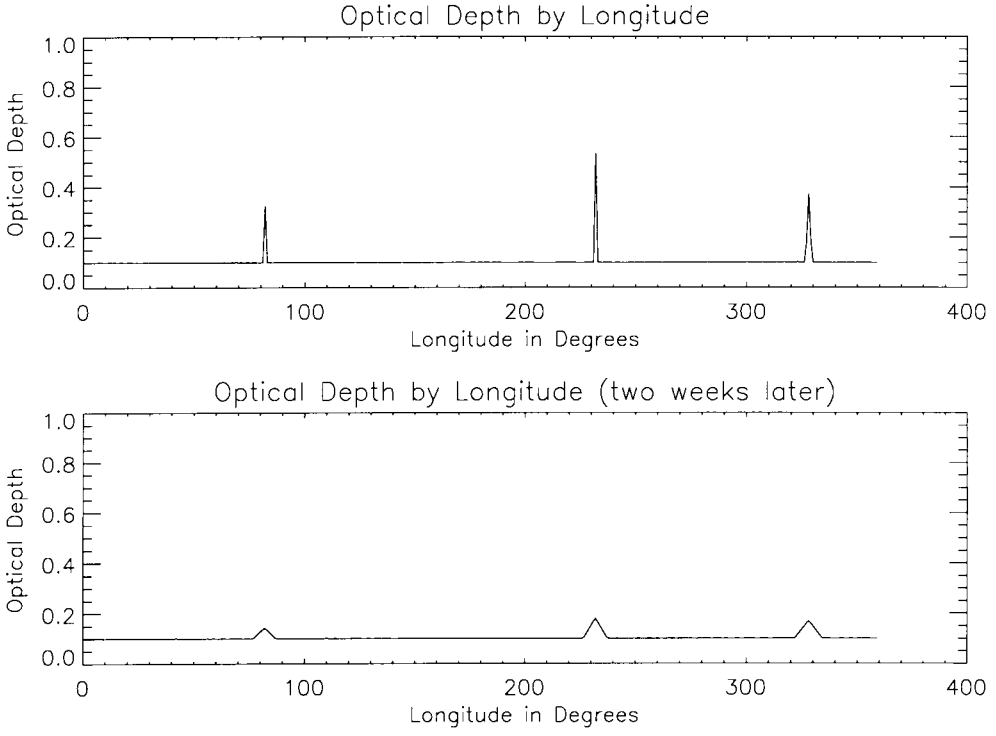

FIG. 7. Representative results from the moonlet collision model (for $q_{\text{ejecta}} = 3.1$) where optical depth, τ, is plotted as a function of longitude. Events are then evolved for two weeks (bottom).

TABLE I
Model Results

v_{rel}[a] (m s^{-1})	q_{ejecta}[b]	N_m[c]	R_u[d] (km)	τ_{mb}[e]	N_{events}[f]	$\Delta\tau/\tau$[g]	R_{eq}[h] (km)
1	2.5	Thousands	10	10^{-3}	Hundreds	0–1	100
	3.1	~100	8	10^{-4}	0–4	1–7	30
	3.5	0	NA	0	0	NA	7
5	2.5	Thousands	10	10^{-3}	Hundreds	0–1	100
	3.1	~100	8	10^{-4}	4–10	1–7	30
	3.5	0	NA	0	0	NA	7
10	2.5	Thousands	10	10^{-3}	Hundreds	0–1	100
	3.1	~100	8	10^{-4}	10–20	1–7	30
	3.5	0	NA	0	0	NA	7

Note. In each case, overall ring mass has been modified such that average optical depths for the F ring remain at or close to 0.1.

[a] Relative collision velocity.

[b] Exponent for the power law (in terms of radius) according to which mass is redistributed after a disruptive collision.

[c] Approximate total number of objects contained in the moonlet belt.

[d] Approximate radius of the largest moonlet present in the belt assuming a particle density of 1000 kg m^{-3}.

[e] Average moonlet belt optical depth.

[f] Typical number of events.

[g] Brightness of an event where $\Delta\tau$ is the difference in optical depth between the clump and the average optical depth for the ring, τ.

[h] Equivalent radius of a single hypothetical F-ring progenitor assuming density equal to 1000 kg m^{-3}.

measured spreading rate of these events requires collision velocity $v_{rel} > 4$ m/s (Showalter 1998). These higher velocities could not characterize all collisions among F-ring and other particles between the two shepherds, but only the most energetic. For $1 \le v_{rel} \le 10$ m s^{-1} (see Fig. 9), we find that q_{ejecta} close to 3 produces results most consistent with observations made during the 1995 ring-plane crossings as well as those made by *Voyager* (i.e., just a few visible clumps present in the F ring at any given time). Values less than 3 generate belts containing thousands of moonlets, in turn producing hundreds of visible events. Values substantially greater than 3 create belts containing little or no moonlets, and pronounced events are sparse or absent entirely (see Table I, where in each case overall ring mass has been modified such that average optical depth for the F ring remains at or close to 0.1).

For our best value, $q_{ejecta} \approxeq 3$, the final steady-state distribution of ring particles deviates sharply from the continuous power law after reaching a radius of ~200 m. Minimum values for mass and number of moonlet belt objects occur in the range 500–600 m, and moonlets with radii on the order of 1–3 km persist in fairly equal numbers, far greater than those predicted by one continuous power-law distribution. The largest moonlet created in this scenario has a radius of approximately 8 km—below the detection capabilities of *Voyager*'s cameras. Also included in Table I are calculated average optical depths for the moonlet population, which are in good agreement with τ estimates of order 10^{-4} to 10^{-3} by Cuzzi and Burns (1988). These opacity values would be undetectable by the *Voyager* occultations. Event intensities

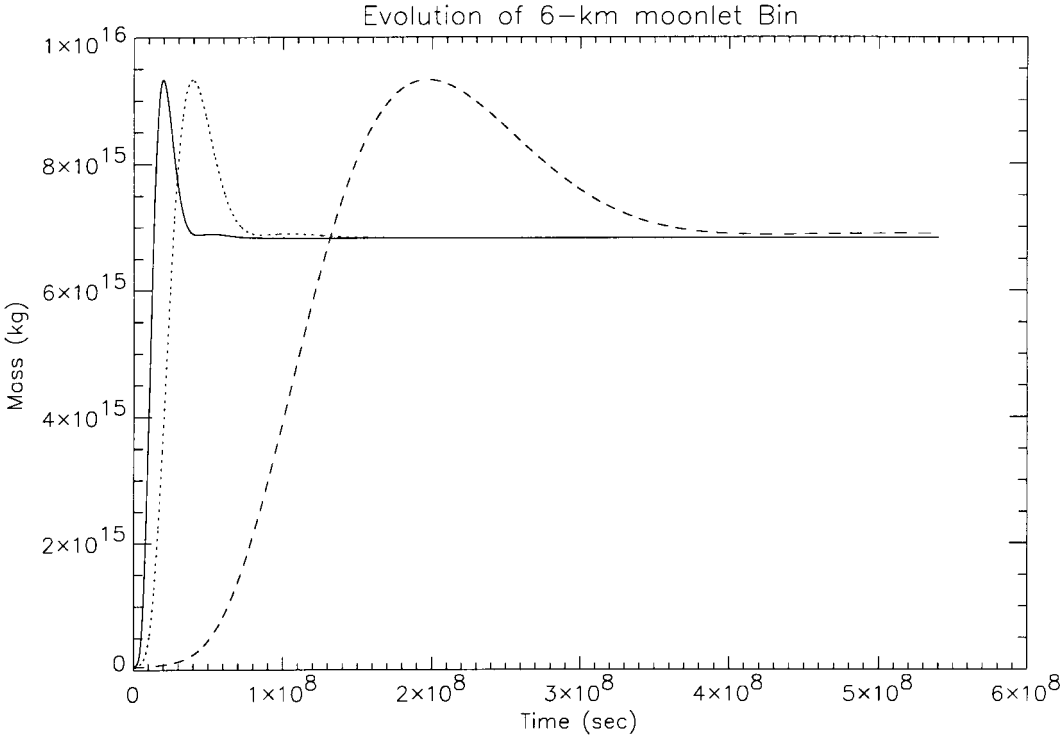

FIG. 8. Rate of evolution toward equilibrium in the ~8-km-radius moonlet bin for $v_{rel} = 10$ (solid), 5 (dotted), and 1 m s^{-1} (dashed).

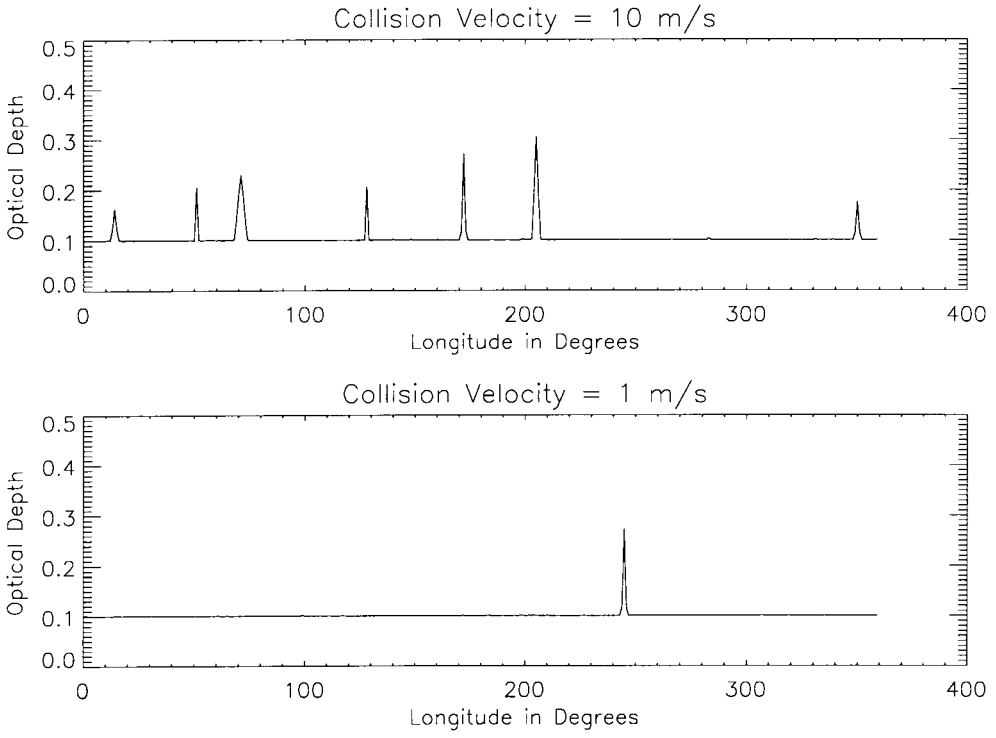

FIG. 9. Relationship between relative collision velocities for colliding particles and event frequency for 10 (top) and 1 m s^{-1} (bottom).

generated by our simulation are also in excellent agreement with the photometric analysis conducted by Poulet *et al*. (2000), who were able to constrain the local contrast in brightness for three of the new objects, S5, S6, and S7, from Hubble Space Telescope images obtained 10 August 1995. They describe brightness as $\Delta\tau/\tau$ where $\Delta\tau$ is the difference in optical depth between the clump and the average optical depth for the ring, τ. For objects S5, S6, and S7, Poulet *et al*. obtain typical values between 2 and 3 for the local brightness contrast. We find $5 \leq \Delta\tau/\tau \leq 10$ for $q_{\text{ejecta}} \geq 3.2$, $1 \leq \Delta\tau/\tau \leq 5$ for $3.0 \leq q_{\text{ejecta}} \leq 3.2$, and values at or below 1 for $q_{\text{ejecta}} \leq 3.0$.

5. CONCLUSIONS

The numerical simulation presented here considers only the region referred to as the "classical F ring." However, as suggested by Cuzzi and Burns (1988), this moonlet belt may stretch throughout the region between the orbits of Prometheus and Pandora, which can explain why the F ring is not centered in force balance between the shepherding moons—within this framework it is the moonlet belt rather than the F ring itself, maintaining and transferring torques. In agreement with Cuzzi and Burns, we contend that the F ring may in fact be transient, and merely the progeny of one of the moonlets of this broader moonlet belt. Therefore, specifically, we see the model presented in this manuscript as a first estimate of this broader population. Those large bodies whose orbits bring them close to the ring may also contribute to some of the more stable "kinks" in the ring. The F ring is very efficient at forward-scattering visible light, indicative of the presence of large amounts of micrometer-sized dust particles. Strands may result from gravitational perturbations from the largest members of the moonlet belt as well as from the F ring's shepherds. Constant collisions within these strands can produce the large amounts of observed micrometer-sized dust particles. In addition to the F ring's shepherds, Prometheus and Pandora, the largest moonlets within this belt may also cause some of these relatively stable structures.

The *Voyager* encounters have offered detailed information regarding the precise orbital parameters of Prometheus and Pandora. However, observations made in 1996 revealed that Prometheus had wandered some 20° from its well-predicted location. We agree with Showalter (1999), who has suggested that this discrepancy between the predicted and observed locations of Prometheus may also be explained in terms of resultant gravitational perturbations from encounters with large nearby moonlets.

Constraining the flux of meteoroids in the outer Solar System is imperative to understanding the evolution of planetary ring and moon surfaces. However, the meteoroid impact model for burst events predicts many more smaller-scale events than were detected by *Voyager*. This inconsistency with observation is a direct result of the steep power-law distribution of impacting meteoroids. While, admittedly, many of these smaller events would remain hidden within the noise and complex structure of the F ring, we contend that it would be difficult to hide all of the abundant dimmer events. In contrast, the moonlet collision model presented here predicts only a few relatively large events. We predict that detailed images of small moons and transient F-ring

features made with the *Cassini Orbiter* spacecraft would show high relative velocities for the moonlets and an absence of small burst events relative to large events like those seen by *Voyager*.

The F ring's distance from its host planet, beyond the classical Roche limit, places it in a unique transitional location somewhere between planetary ring and moon regimes, a location that demands thorough consideration of both the processes of accretion and disruption. We have developed a simple evolutionary model consistent with general collision models and supportive of other works involving tidally modified accretion. The model is quite similar to that of Poulet *et al.* (2000) with the exception that we explicitly consider the evolution of a complete size distribution under the effects of both accretion and fragmentation in the F ring. The major conclusions drawn from the numerical moonlet collision model are that (1) an initially continuous size distribution of ring particles subjected to the competing effects of accretion and disruption in this "tidally modified" region evolves toward a bimodal size distribution; (2) the larger mode of the final state distribution represents a belt of kilometer-sized moonlets reminiscent of that first hypothesized by Cuzzi and Burns (1988); and (3) the complete disruption of these loosely bound larger moonlets can give rise to the burst events witnessed by Showalter, and to the visually prominent transient features later observed during the Earth and Sun crossings of Saturn's ring plane.

In agreement with Cuzzi and Burns (1988), we also suggest that the classical F ring may itself be transient, and only the result of a relatively recent collision involving two of the largest parent bodies present in the ring. The presence of a population of moonlets also offers a reasonable explanation for the apparent wandering of Prometheus and Pandora (Esposito 2002).

ACKNOWLEDGMENTS

Thanks to Joshua Colwell, Glen Stewart, and other members of the Colorado rings group for helpful discussions, and to Mark Showalter and an anonymous referee for their careful reviews and helpful suggestions. Support for this work was provided by NASA through JPL Contract 961196, Cassini–Huygens Mission to Saturn and Titan.

REFERENCES

Asphaug, E., S. J. Ostro, R. S. Hudson, D. J. Scheeres, and W. Benz 1998. Disruption of kilometre-sized asteroids by energetic collisions. *Nature* **393**, 437–440.

Burns, J. A. 1999. Planetary rings. In *The New Solar System* (J. K. Beatty, C. C. Peterson, and A. Chaikin, Eds.), pp. 221–240. Sky Publishing, MA, and Cambridge Univ. Press, Cambridge, UK.

Canup, R. M., and L. W. Esposito 1995. Accretion in the Roche Zone: Coexistence of rings and ringmoons. *Icarus* **113**, 331–352.

Canup, R. M., J. E. Colwell, and M. Horanyi 1993. Size distributions of satellite dust ejecta: Effects of radiation pressure and planetary oblateness. *Icarus* **105**, 363–369.

Colwell, J. E. 1993. A general formulation for the distribution of impacts and ejecta from small planetary satellites. *Icarus* **106**, 536–548.

Colwell, J. E. 1994. The disruption of planetary satellites and the creation of planetary rings. *Planet. Space Sci.* **42**, 1139–1149.

Colwell, J. E. 1996. Size distribution of circumplanetary dust. *Adv. Space Res.* **17**, 161–170.

Colwell, J. E., and L. W. Esposito 1990a. A model of dust production in the Neptune ring system. *Geophys. Res. Lett.* **17**, 1741–1744.

Colwell, J. E., and L. W. Esposito 1990b. A numerical model of the uranian dust rings. *Icarus* **86**, 530–560.

Colwell, J. E., and L. W. Esposito 1992. Origins of the rings of Uranus and Neptune. 1. Statistics of satellite disruptions. *J. Geophys. Res.* **97**, 10,227–10,241.

Cuzzi, J. N., and J. A. Burns 1988. Charged particle depletion surrounding Saturn's dusty F ring: Evidence for a moonlet belt? *Icarus* **74**, 284–324.

Cuzzi, J. N., and R. H. Durisen 1990. Bombardment of planetary rings by meteoroids: General formulation and effects of Oort cloud projectiles. *Icarus* **84**, 467–501.

Cuzzi, J. N., and L. W. Esposito 1987. The rings of Uranus. *Sci. Am.* **255**, 52–66.

Esposito, L. W. 2002. Drunken shepherds: Random walk models for Pandora and Prometheus. European Geophysical Society Abstracts, Vol. 4, 27th General Assembly, EGS02-A-05215.

Esposito, L. W., J. E. Colwell, and W. E. McClintock 1998. Cassini UVIS observations of Saturn's rings. *Planet. Space Sci.* **46**, 1221–1235.

Gehrels, T., L. R. Baker, E. Beshore, C. Blenman, J. J. Burke, N. D. Castillo, B. Da Costa, J. Degewij, L. R. Doose, J. W. Fountain, J. Gotobed, C. E. KenKnight, R. Kingston, G. McLaughlin, R. McMillan, R. Murphy, P. H. Smith, C. P. Stoll, R. N. Strickland, M. G. Tomasko, M. P. Wijesinghe, D. L. Coffeen, and L. W. Esposito 1980. Imaging photopolarimeter on Pioneer Saturn. *Science* **207**, 434–439.

Harris, A. W. 1998. Making and breaking asteroids. *Nature* **393**, 418–419.

Hartmann, W. K. 1969. Terrestrial, lunar, and interplanetary rock fragmentation. *Icarus* **10**, 201–213.

Kolvoord, R. A., J. A. Burns, and M. R. Showalter 1990. Periodic features in Saturn's F ring: Evidence for nearby moonlets. *Nature* **345**, 695–697.

Martelli, G., E. V. Ryan, A. M. Nakamura, and I. Giblin 1994. Catastrophic disruption experiments: Recent results. *Planet. Space Sci.* **42**, 1013–1026.

Ohtsuki, K. 1993. Capture probability of colliding planetesimals: Dynamical constraints on accretion of planets, satellites, and ring particles. *Icarus* **106**, 228–246.

Poulet, F., B. Sicardy, P. Nicholson, E. Karkoschka, and J. Caldwell 2000. Saturn's ring-plane crossings of August and November 1995: A model for the new F-ring objects. *Icarus* **144**, 135–148.

Roddier, F., C. Roddier, A. Brahic, C. Dumas, J. E. Graves, M. J. Northcott, and T. Owen 2000. Adaptive optics observations of Saturn's ring plane crossing in August 1995. *Icarus* **143**, 299–307.

Showalter, M. R. 1992. A photometric study of Saturn's F ring. *Icarus* **100**, 394–411.

Showalter, M. R. 1993. Seeing ghosts: Photometry of Saturn's G ring. *Icarus* **103**, 124–143.

Showalter, M. R. 1998. Detection of centimeter-sized meteoroid impact events in Saturn's F Ring. *Science* **282**, 1099–1102.

Showalter, M. R. 1999. Revenge of the sheep: Effects of Saturn's F ring on the orbit of Prometheus. *Bull. Am. Astron. Soc.* **31**, 1141. [Abstract 44.08]

Smith, B. A., L. Soderblom, R. Batson, P. Bridges, J. Inge, H. Masursky, E. Shoemaker, R. Beebe, J. Boyce, G. Briggs, A. Bunker, S. A. Collins, C. J. Hansen, T. V. Johnson, J. L. Mitchell, R. J. Terrile, A. F. Cook, J. Cuzzi, J. B. Pollack, G. E. Danielson, A. P. Ingersoll, M. E. Davies, G. E. Hunt, D. Morrison, T. Owen, C. Sagan, J. Veverka, R. Strom, and V. E. Suomi 1982. A new look at the Saturn system. *Science* **215**, 504–537.

Stewart, G. R., and G. W. Wetherill 1988. Evolution of planetesimal velocities. *Icarus* **74**, 542–553.

Throop, H. B., and L. W. Esposito 1998. G ring particle sizes derived from ring plane crossing observations. *Icarus* **131**, 152–166.